A COMPARATIVE STUDY OF BLOB DETECTION METHODS: EVALUATION ON NODULE CANDIDATE DETECTION IN CHEST RADIOGRAPHS

A Thesis

Submitted to

The School of Engineering of the

UNIVERSITY OF DAYTON

In Partial Fulfillment of the Requirements for

The Degree

Master of Science in Electrical Engineering

by

Bernard Olushola Abayowa

UNIVERSITY OF DAYTON

Dayton, Ohio

May 2008

A COMPARATIVE STUDY OF BLOB DETECTION METHODS: EVALUATION ON NODULE CANDIDATE DETECTION IN CHEST RADIOGRAPHS

APPROVED BY:

Russell Hardie, Ph.D.
Advisor Committee Chairman
Department of Electrical and
Computer Engineering

John Loomis, Ph.D.
Committee Member
Department of Electrical and
Computer Engineering

Raúl Ordóñez, Ph.D.
Committee Member
Department of Electrical and
Computer Engineering

Malcolm W. Daniels, Ph.D.
Associate Dean
School of Engineering

Joseph E. Saliba, Ph.D., P.E.
Dean
School of Engineering

ABSTRACT

A COMPARATIVE STUDY OF BLOB DETECTION METHODS: EVALUATION ON NODULE CANDIDATE DETECTION IN CHEST RADIOGRAPHS

Name: Abayowa, Bernard Olushola
University of Dayton

Advisor: Dr. Russell Hardie

In some pattern recognition applications, simple blob detection is used to identify candidate objects of interest in a full image. The detected candidate blobs are then further scrutinized and ultimately classified in subsequent stages of a pattern recognition system. The main focus of this paper is on the detection of nodule candidates in chest radiographs. Lung cancer is a major cause of cancer mortality and early detection of lung nodules can potentially save lives. Computer-aided detection (CAD) systems have proven to help radiologists increase detection rate of small pulmonary nodules in chest radiographs.

This thesis provides a formal performance comparison of some of the recently proposed nodule candidate detectors for the selection of initial nodule candidates in chest radiographs in both the non-opaque and opaque portions of the lung. The nodule candidate detectors evaluated in this paper include the Lindeberg blob detector, the average radial gradient detector and variations of the convergence index based detectors. This thesis also describes a method for segmenting the opaque region of the lung in a chest radiograph based on

a segmentation of the non-opaque portion. A method for optimizing some of the multi-parameter blob detectors using genetic algorithms is also presented in this thesis. Finally, an analysis to aid in selecting an operating point for the detector in both regions to achieve a desired overall sensitivity and specificity is presented.

Dedication

This thesis is dedicated to my father the late Mr. Michael Abayowa, my mother Mrs. Victoria Abayowa, my advisor Dr. Russell Hardie, The Dayton Area Graduate Studies Institute (DAGSI), and my dearest friends for all their support and encouragement.

TABLE OF CONTENTS

LIST OF FIGURES

LIST OF TABLES

CHAPTER I

Introduction

There are many applications in pattern recognition where one seeks to detect compact objects or "blobs" in an image. One such application is in the detection of lung nodules in chest radiographs [1–7]. Several papers about blob detectors and their applications can be found in the literature. Lindeberg [8, 9] presents a technique for extracting blob-like structures and their scales from images. Moreover in [10], Chang *et al* proposes a method for segmenting heterogeneous blob objects by combining voting, Voronoi tessellation, and level set methods. Other blob detection work can be found in [11–15] and [16].

In some applications, simple blob detection is used to identify candidate objects of interest in a full image. The detected candidate blobs are then further scrutinized and ultimately classified in subsequent stages of a pattern recognition system. A good candidate detection scheme, based on blob detection, has a high sensitivity and specificity. We wish to detect as many targets as possible with as few false positive detections as possible (since each detection will require further processing and computational resources). Thus, blob detection may serve as a key screening step in many pattern recognition problems. As such these detectors can have a significant impact on the overall performance and computational complexity of a pattern recognition system.

In this thesis, we focus on the application of blob detection to lung nodule detection in chest radiographs. Lung nodules are potentially cancerous lesions that are roughly elliptical in shape (often blob like). This is a problem of great importance. Lung cancer is a major cause of cancer mortality and early detection of lung nodules can potentially save lives. Generally, computed tomography is preferable to chest radiography in early detection of lung nodules [17]. However, it usually generates numerous false positives which can lead to unnecessary surgical lung biopsy. Moreover, chest radiography still remains the most commonly used procedure for lung nodule diagnosis because of its low cost and low dose. Reports from a survey on computer-aided diagnosis in chest radiography in [18] shows that nodule detection in chest radiographs is still a difficult task in computer aided diagnosis.

A typical CAD system for identifying lung nodules in chest radiographs consists of the components shown in Figure 1.1. The system generally begins with a preprocessor where the input image is treated to reduce processing time and make the pulmonary nodules more detectable, while reducing number false detections as well. The next component is usually a blob detector used to identify lung nodule candidates. The next part in the CAD system is the nodule segmentation step. The purpose of the nodule segmentation step is to delineate the boundary of candidate nodule to allow for subsequent feature extraction. Finally, a classifier is used to make the final decision regarding each candidate.

The use of blob detection for the nodule candidate detector component is the main focus of this thesis. This component is key to the overall CAD system and it governs the overall system's sensitivity and the computational demands of the system (in terms of the number of candidates to be subsequently processed). Several methods have been proposed for the detection of initial nodule candidates in lung nodule CAD systems. However, no formal

Figure 1.1: A block diagram of a Typical CAD system showing the stages involved in the pattern recognition system. The candidate detection step often uses a simple blob detector and this component is the focus of the present thesis.

comparison has been done to evaluate the performance of these detectors. Moreover, some of these detectors require several tuning parameters which are often selected using ad hoc methods. Another important issue with lung nodule detection relates to the location of the nodule on the chest radiograph. Sometimes nodules appear in the retrocardiac and subdiaphragmatic area of the lung (as in [1, 2, 7], we refer to these as opaque regions on the radiograph). In many of the proposed CAD systems, nodules in the opaque region of the lung are excluded from analysis or considered as missed detections in the overall performance analysis of the CAD system.

This thesis provides a formal performance comparison of some of the recently proposed candidate detectors for the selection of initial nodule candidates in chest radiographs in both the non-opaque and opaque portions of the lung. We describe a method for segmenting the opaque region of the lung in a chest radiograph based on a segmentation of the non-opaque portion. We also provide an analysis to aid in selecting an operating point for the detector in both regions to achieve a desired overall sensitivity and specificity. Another contribution of this thesis is we propose a method for optimizing some of the multi-parameter blob detectors using genetic algorithms.

Six nodule candidate detectors recently proposed in the literature are evaluated in this thesis. The Lindeberg blob detector, which uses the Laplacian of Gaussian (LoG) filter, is discussed. Our implementation of the Lindeberg detector is similar to that of [3]. Moreover an average radial gradient (ARG) detector, similar to that described in [1], is implemented and evaluated. Four variations of the convergence index (CI) based detectors are also implemented and evaluated. The CI based detectors include the Single disk convergence index (SDCI) detector and the ring convergence index (RCI)detector [4]. Finally, the weighted convergence index (WCI) detector and weighted multi-scale convergence index (WMCI) detector, proposed in [7], are also evaluated. Since the WCI and WMCI have a large number of tuning parameters, here we present a genetic algorithms for optimally selecting these parameters.

We employed two chest radiograph databases in this study, one for optimizing the detector tuning parameters and an independent one for testing. The nodule candidate detectors are trained using data provided by Riverain Medical Group (RMG) [1] and are tested using an independent data set from the Japanese Society of Radiological Technology (JRST) database. The RMG training set is comprise of 153 nodule cases with 6 of the nodules located in the opaque region, and 147 of the nodules located in the non-opaque region of the lung. The nodule sizes for this set ranges between 8 to 30 mm in diameter. This RMG set represents a sampling from Riverain's database and consists of a mix of computed radiography images, digital radiography images and digitized film images. The performance of nodule candidate detectors analyzed are tested on the JRST database. The JRST database is a publicly available database which contains 247 chest radiographs which are of size 2048

[1]Riverain Medical, 3020 South Tech Boulevard Miamisburg, Ohio 45342-4860. Maker of the FDA approved RapidScreen® lung CAD system.

x 2048 pixels with pixel spacing of 0.175 mm and 4096 gray scale levels. Out of these 247 chest radiographs, 93 cases do not contain lung nodules and are therefore excluded from this analysis. The 154 cases, with one nodule each, consist of 100 malignant cases and 54 benign cases. The nodule sizes for the cases with proven nodule ranges between 5 to 60 mm in diameter. The JRST data lung nodule cases database contain 14 chest radiographs that appear in the opaque region of the lung. The chest radiographs which contain nodules in this region of the lung are analyzed separately.

The rest of the thesis is arranged as follows. In Chapter 2, the nodule candidate detectors are introduced. These include the Lindeberg, ARG, SDCI, RCI, WCI and WMCI detectors. This section also includes a description of the preprocessing and postprocessing steps as well as our labeling and scoring methods. In Chapter 3, we describe the optimization of the tuning parameters for the detectors. In particular, we present a novel genetic algorithm based optimization for the tuning parameters for the WCI and WMCI candidate detectors. An exhaustive search is used to optimize the other detector's tuning parameters. The experimental results are then presented in Chapter 4. Here we analyze the performance of the detectors in locating lung nodules in the opaque and nonopaque regions of the chest radiographs. Finally, conclusions follow in Chapter 5.

CHAPTER II

Nodule candidate detection process

This chapter describes the nodule candidate detection process that is used to for training and testing the nodule candidate detectors evaluated in this thesis. The first section describes the preprocessing methods applied to the training and testing data which includes the method used for segmenting the opaque region of the lung. The preprocessing allow for faster processing and reduce false detections while making true nodules more identifiable during nodule candidate selection. Following the description of the preprocessing methods, this chapter introduces the nodule candidate detectors evaluated in this thesis. These nodule candidate detectors include the Lindeberg blob detector which in used in [3], average radial gradient (ARG) filter based detector used in [1] and various form of convergence index (CI) filter based detectors which are employed in [4, 7, 21, 23]. Furthermore, the postprocessing method used for detection thinning as well as the labeling and scoring method are presented. A block diagram showing the nodule candidate detection process is depicted in Figure 2.1

2.1 Preprocessing

The original JRST data are of size 2048 x 2048 pixels with pixel spacing of 0.175 mm and 4096 gray scale levels. The data is resampled to 0.7 mm, which corresponds to images

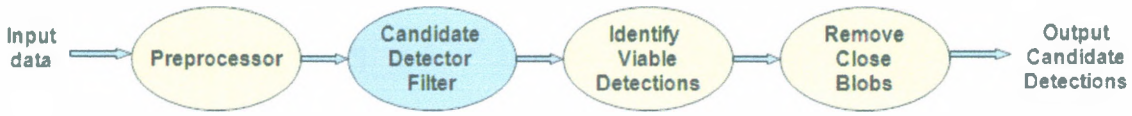

Figure 2.1: Candidate Detector Block Diagram

of size 512 x 512, using bilinear interpolation. The image is then normalized using the mean and standard deviation information of each image. An example of the resized image is shown in Figure. 2.2

The contrast across different images and within each image in the JRST data is normalized using a local contrast enhancement (LCE) algorithm similar to that in [2, 3, 7]. The LCE algorithm involves normalizing the local mean and standard deviation of each image using a large Gaussian convolution kernel. The LCE operation is defined as

$$y(m,n) = \frac{x(m,n) - \mu(m,n)}{\sigma(m,n)}, \tag{2.1}$$

where $x(m,n)$ is the input image, $y(m,n)$ is the LCE image, $\mu(m,n)$ is a local mean estimate, and $\sigma(m,n)$ is a local standard deviation estimate. The local mean $\mu(m,n)$ is generated by convolving the input image with a Gaussian low-pass filter. The Gaussian low-pass filter's impulse response function has a standard deviation of 16. The local standard deviation estimate $\sigma(m,n)$ is generated as

$$\sigma(m,n) = \sqrt{x^2(m,n) * h(m,n) - \mu^2(m,n)}. \tag{2.2}$$

The local contrast enhanced image is used for training and testing each candidate detector analyzed in this report. An example showing an LCE image is shown in Figure. 2.3

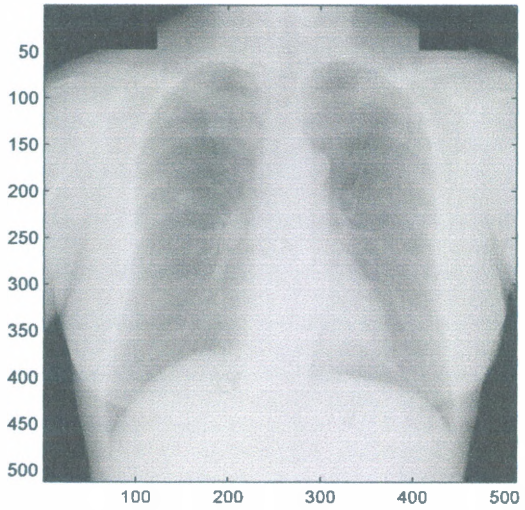

Figure 2.2: Typical resized image (JPCLN004). This image is resized from 2048 x 2048 pixels with pixel spacing of 0.175 mm to a pixel spacing of 512 x 512 with 0.7 mm pixel spacing

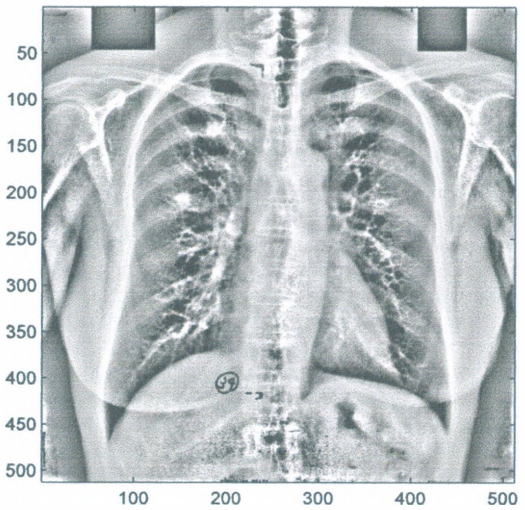

Figure 2.3: Typical Local Contrast Enhanced Image (JPCLN004)

To allow for labeling and scoring of the nodule candidate detectors, the lung nodules in each chest radiographs are manually segmented based on the truth cue point and size provided for each image in the JRST and RMG databases. To avoid detections in regions of the chest radiograph where lung nodules do not occur, a nodule search area is defined for each chest radiograph. The nodule search area for cases with nodules in the non-opaque region of the lung are defined using manual lung masks. Manual lung masks is provided along with the RMG data. The JRST database manual lung masks made available from the work in [19] is used to limit the search region in JRST lung nodule cases. The manual segmentations in [19] also include segmentations of other anatomical structures like the heart and the clavicle. An automated segmentation of the non-opaque region of the lung can be done using an active shape model (ASM) as in [7, 19]. An example showing an LCE image with the manual nodule mask, lungs, heart, and clavicle segmentation is depicted in Figure. 2.4. All the mask are added to the preprocessed image to show locations of the lungs, heart and clavicle in each image.

Opaque region segmentation The nodule search area for cases with nodules in the opaque region of the lung is defined by automatically segmenting the region using four points (A, B, C and D) on the the non-opaque region manual lung mask boundary as guidance. An example of the automatic segmentation covering the retrocardiac and subdiaphragmatic region of the lung with points A, B, C and D used for segmentation is depicted in figure 2.5. For the left lung, the closest point to the heart on the horizontal (point B), and the farthest point from the diaphragm on the vertical (point A) is located in the left lung masks. A straight line is then drawn towards each other until the two points intersect (horizontal line from A and vertical line from point B). The opaque region is then defined as

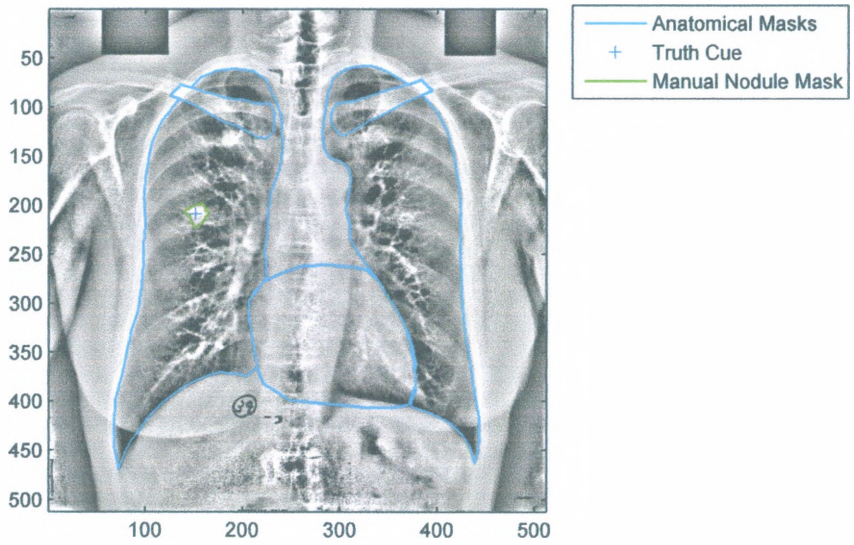

Figure 2.4: Typical LCE image showing image masks (JPCLN004). The Anatomical masks consist of the heart, left and right clavicle and the left and right lungs. The truth cue is provided for each image as selected by the radiologist. The nodule mask is manually segmented taking the size of the nodule into consideration.

the area outside of the lung mask and in the right angle triangle formed by the intersection of point A and point B. The same procedure is repeated for the right lung using points C and D and the manual non-opaque region lung mask for the right lung. This segmentation method sufficiently covers the opaque region of the lung for all nodules in this study.

2.2 Nodule candidate detectors

This section provides a detailed description of some of the candidate detectors that are used for the selection of initial nodules in chest radiographs. The nodule candidate

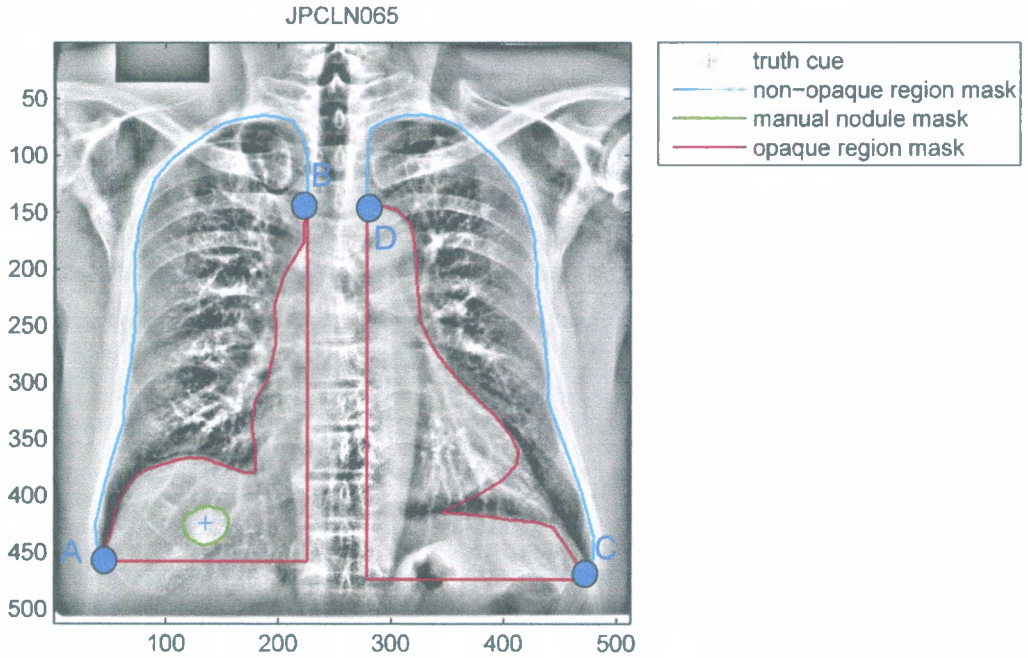

Figure 2.5: An example of the automatic segmentation covering the retrocardiac and sub-diaphragmatic region of the lung (JPCLN065).

detectors that are described include the Lindeberg, ARG, SDCI, RCI, WCI and WMCI detectors.

2.2.1 Lindeberg blob detector

The Lindeberg blob detector is based on the Laplacian of Gaussian (LoG) filter. The Laplacian filter is a convolution filter that yields high responses to regions of an image with rapid intensity changes. It is therefore used for edge detection in images. The Gaussian filter is used to smooth an image while preserving edges. The LoG filter applies a Gaussian

blur at different scales to the input image in conjunction with a Laplacian filter to generate output images at various scales. Given a 2D image $f(x, y)$, The Laplacian is defined as

$$\Delta f(x, y) = \frac{\partial^2 f}{\partial x^2} + \frac{\partial^2 f}{\partial y^2}. \tag{2.3}$$

The Gaussian kernel at scale t is defined as

$$\mathrm{g(x, y, t)} = \frac{1}{2\pi \mathrm{t}} e^{-\frac{(x^2+y^2)}{2t}}. \tag{2.4}$$

The Lindeberg blob detector identifies blobs by generating a gamma-normalized scale space from the input image using a scale-normalized LoG operator as described in [9]. Based on the above definitions of the Guassian and Laplacian filters, the Lindeberg blob detector is given by

$$\Delta_{norm} L(x, y; t) = t \left(\frac{\partial^2 L}{\partial x^2} + \frac{\partial^2 L}{\partial y^2} \right), \tag{2.5}$$

where L(x,y;t) is the result of the convolution of a Gaussian kernel at scale t with the input image $f(x, y)$. The result of the Lindeberg blob detector on a chest radiograph is a stack of images where each image represents the result of the Laplacian of Gaussian operation at each scale t, with positive responses on nodules at that scale.

The implementation of the Lindeberg detector is similar to that of [3]. The Laplacian of the input image is pre-computed and then Gaussian kernels at different scales (variances) are successively applied to the Laplacian output. A combination of 5 scales are selected from scale range $1 \leq \sigma \leq 16$ mm by training on the riverain preprocessed data using exhaustive search. The 5 scale selection that yielded the highest performance on the training set are used in testing the detector on JRST data. A total of 4368 combinations of scales are generated in the range $1 \leq \sigma \leq 16$ mm, by putting together all the 5 combination

possible out of the 16 numbers. During each iteration a local contrast enhanced chest radiograph is loaded and convolved with one of the commonly used spatial approximation of the Laplacian filter. The discrete approximation of the Laplacian impulse response, convolved with the chest radiographs, has a value of 1 in the center and $-1/4$ on all four sides of the central point as shown in Figure 2.7. The output is the gradient magnitude approximation of the second derivative at each pixel intensity in the local contrast enhanced chest radiograph. Moreover, 5 versions of the image is generated by convolving the output of the Laplacian filtered image with five gaussian kernels. The variance for the gaussian kernels are chosen from the 4368 combination of scales generated, to complete the application of the Laplacian of Gaussian filter on the image.

After the Application of the Laplacian of Gaussian filter, each output image is multiplied by the scale at which they are computed to generate a gamma normalized scale space made up of five images. Postprocessing methods described in Section 2.3 are then applied to the output image to generate the final detections of the Lindeberg detector. The final detection coordinates are selected from all the five scales. The five combination of variances which generated scales that performed best on the training data with nodules in the non-opaque region are 4, 7, 10, 14, and 16 mm. The output of the Laplacian of Gaussian filter at these scales on an example chest radiograph is shown in Figure 2.6. These scales are used to test the performance of the Lindeberg detector on the testing data with nodules in the non-opaque. A similar procedure is repeated for nodules that appear in the opaque region of the lung with scales 7, 9, 11, 13, and 15 mm yielding best results in this region.

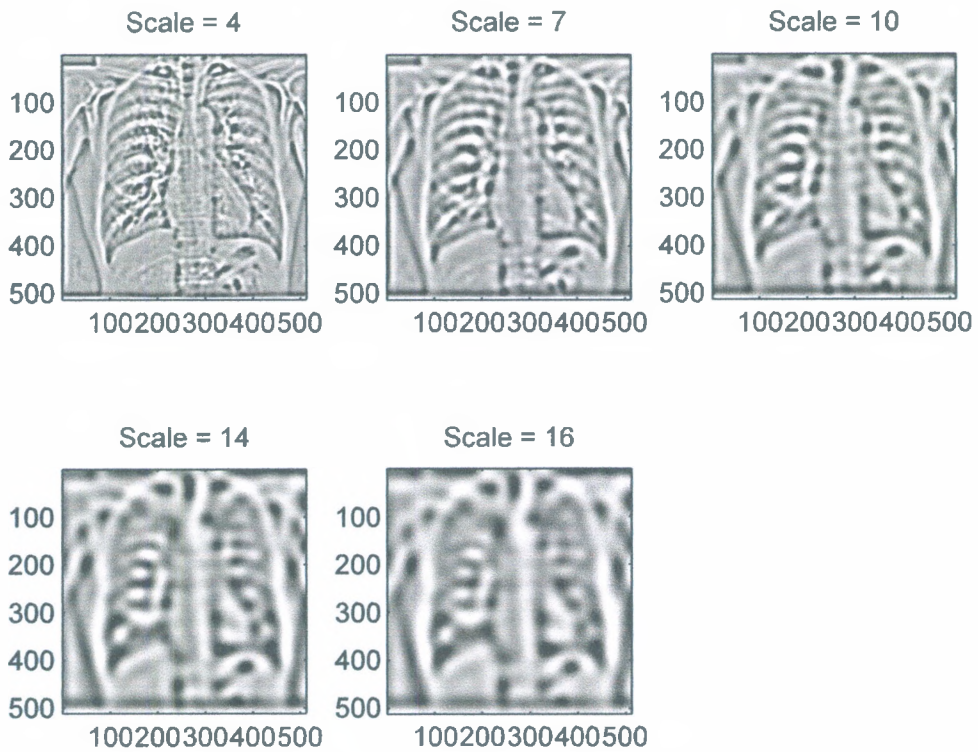

Figure 2.6: Results of the application of the Laplacian of Guassian filter on LCE image JPCLN001 of the JRST database. The scale at which each image is generated is shown at the top of each image.

2.2.2 Average radial gradient (ARG) detector

The intensity gradients of a true nodule are usually oriented towards the center of the nodule where it is brighter. The ARG detector computes the average radial gradient in a circular region specified by a radius r about each pixel in an image. The result is the average of the gradients projected in the radial direction for pixels in the defined region

$$\begin{bmatrix} 0 & -\frac{1}{4} & 0 \\ -\frac{1}{4} & 1 & -\frac{1}{4} \\ 0 & -\frac{1}{4} & 0 \end{bmatrix}$$

Figure 2.7: A discrete approximation of the Laplacian filter.

about each pixel. The ARG value is obtained from the magnitude and angle information of the average radial gradient.

Given a circular region on a two dimensional (2D) space denoted by R, and a pixel of interest located at the center of this region denoted by (m, n), the average radial gradient value at pixel (m, n) is the average of $|g(m+k, n+l)|\cos(\theta_{m,n}(k, l))$ for $(k, l) \in R$ and is given by

$$ARG(m, n) = \frac{1}{M} \sum_{(k,l)\in R} |g(m+k, n+l)| \cos(\theta_{m,n}(k, l)), \tag{2.6}$$

as proposed in [1] where $\theta_{m,n}(k, l)$ is the angle between the radial vector pointing from pixel $(m+k, n+l)$ to (m, n) and the intensity gradient vector at pixel $(m+k, n+l)$, $|g(m+k, n+l)|$ is the magnitude of the local gradient at the pixel $(m+k, n+l)$, and M is the total number of pixels in the region of interest as shown in Figure. 2.8.

The region size selection that yielded highest performance on the training data set is used for testing on JRST data. The region size is defined by radius in the range $1 \leq r \leq 20$

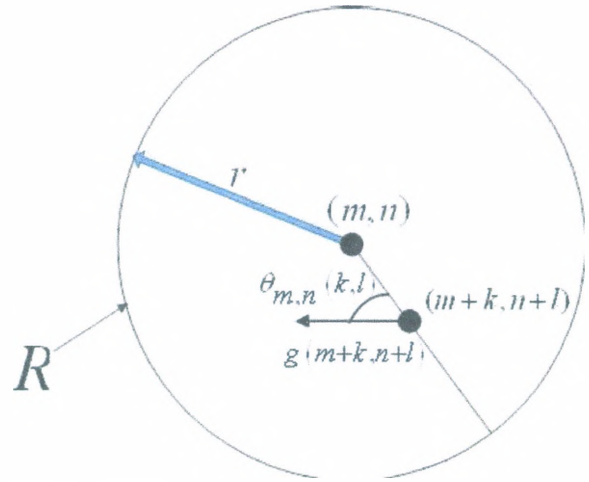

Figure 2.8: Average radial gradient (ARG) and convergence index (CI) value computation. $\theta_{m,n}(k,l)$ is the angle between the radial vector pointing from pixel $(m+k, n+l)$ to (m,n) and the intensity gradient vector at pixel $(m+k, n+l)$, $|g(m+k, n+l)|$ is the magnitude of the local gradient at the pixel $(m+k, n+l)$. R is the region around pixel (m,n) for which the ARG or CI value is computed. The magnitude of the local gradient is not considered when computing CI value.

mm. The optimal region size on the training data set is used to test the JRST data in combination with other fixed tuning parameters. The selection of the optimum region size radius filter used for testing the ARG detector on the JRST data, is selected by training the ARG detector, using all the radii in the range $1 \leq r \leq 20$ mm one after the other, on the training data. Furthermore, postprocessing methods described in Section 2.3 are applied to each of the average radial gradient images generated by each radii to remove false detections. After training the ARG detector on the training data using all the circular radial filters defined by the 20 radii sizes. A radial filter generated by 7 mm radius outperforms other filters, and is used in testing the JRST database for nodules that appear in the non-opaque region of the lung. The same procedure is repeated for nodules that appear in the

opaque region of the lung with the same radial filter of 7 mm outperforming filters with other radii sizes in the defined range.

2.2.3 Convergence index (CI) filter based detectors

The radiographic profile of a nodule can be modeled as a rounded convex region with similar concentric density contours. This implies that each of these rounded convex region points to the center of the nodule as described in [4]. Local regions with most gradient vectors directed towards the center are more likely to be nodule candidates. The CI filter measures the the average angular deviation from radial direction for all gradients in a circle of specified radius about each pixel in an image. Unlike the ARG detector filter, the gradient magnitude information is not included in the computation of the CI value. Given a circular region on a two dimensional (2D) space denoted by R, and a pixel of interest located at the center of this region denoted by (m, n), The CI value at pixel (m, n) is the average of $\cos(\theta_{m,n}(k, l))$ for $(k, l) \in R$ and is given by

$$CI(m, n) = \frac{1}{M} \sum_{(k,l) \in R} \cos\left(\theta_{m,n}(k, l)\right), \tag{2.7}$$

as proposed in [21]; where $\theta_{m,n}(k, l)$ is the angle between the radial vector pointing from pixel $(m + k, n + l)$ to (m, n) and the intensity gradient vector at pixel $(m + k, n + l)$, and M is the total number of pixels in the Region of interest as shown in Figure. 2.8. The output of the CI filter ranges between -1 and +1, where an output of +1 implies all gradient vectors are pointed towards the pixel of interest (m, n) in the center of R.

In this thesis the performance of some of the variations of the CI filter based detector proposed in [4, 5, 7, 21] are analyzed. The variations of the CI filter based detectors analyzed in this thesis are

- Single disk convergence index (SDCI) detector.
- Ring convergence index (RCI)detector.
- Weighted convergence index (WCI) detector.
- Weighted multi-scale convergence index (WMCI) detector.

The processes involved in each CI filter based detector implementation are described below.

Single disk convergence index (SDCI) detector

The single disk convergence index (SDCI) detector uses the CI filter to compute the CI value for each pixel in an image. The region used to generate the CI value for each pixel is specified by a radius which describes the disk being used for detection. The SDCI detector is evaluated in a similar version to the ARG detector. An exhaustive search is performed for an optimal region size specified by the disk radius in the range $1 \leq r \leq 20$ mm. The region size that performed best on the training set is used for testing on JRST data. Though the SDCI detector resembles the ARG detector, there is a difference in the filter computation. As earlier described, the SDCI detector doesn't take the magnitude of the radial gradient into consideration when computing the convergence index value for each point. The SDCI detector is trained using single disk CI filters with various disk sizes determined by the disk radii. A CI image is computed for each chest radiograph. False detections in the CI images are further removed using the postprocessing methods described in Section 2.3. After testing all the various disk sizes in the defined range on the training data. A Single disk CI filter with a radius of 7 mm yielded the best results on lung nodules that appear in

the non-opaque regions of the lung, while a single disk filter with 19 mm radii performed best on the opaque region of the lung.

Ring convergence index (RCI) detector

Another CI filter based detector is the ring convergence index (RCI) detector. The CI value for each region is the CI value from the CI ring filter. The CI ring filter computes the computes the angular deviation from radial for all gradients in a ring about each pixel in the image. The output is the average $\cos(\theta)$ for all gradient angles in the ring. Just like the basic coin filter, the ring filter is independent of gradient magnitude it only takes into consideration the direction information. The RCI value is computed using the convergence index values in a ring R_{r_L,r_U} with lower and upper radii r_L and r_U respectively. The RCI detector is trained using a combination of radii in the range $1 \leq r \leq 20$ mm, using exhaustive search. The radii combination that yielded highest performance is now used for testing the performance of the detector.

A total of 190 radii combinations of two is generated for training the RCI detector on the training data for both opaque and non-opaque regions of the lung. For each of the radii combination, a ring convergence index value is computed for each image. The output for each pixel in an image is the average of the cosine of the radial gradient inside the upper and lower bound ring region around the pixel. After the computation of the RCI value for each image pixel values, false RCI detections are removed using postprocessing methods described in Section 2.3. The upper and lower bound radii values that generated the best results with the RCI detector are $2 \leq r \leq 9$ mm for non-opaque region data and $7 \leq r \leq 19$ mm for opaque region data.

Weighted convergence index (WCI) detector

The weighted convergence index (WCI) detector is another variation of the CI filter detector. The WCI detector extends the SDCI detector by assigning weights to the convergence index value. The WCI value is computed as

$$WCI(m,n) = \sum_{(k,l)\in M} w(k,l)\cos\left(\theta_{m,n}(k,l)\right), \tag{2.8}$$

where $w(k,l)$ is the weight for the gradient angle for position $(m+k, n+l)$ in the window about (m,n). The CI value for each region is computed as the sum of weighted CI values from 4 regions sizes defined by radii in the range $1 \leq r \leq 20$ mm. Genetic algorithm optimization is used to aid in the selection of region sizes defined by 4 radii, and corresponding weights. The genetic algorithm process used for optimizing the tuning parameters for the WCI detector is described in Chapter III. Figures 2.9 and 2.10 shows a depth map of the optimal filter radii with corresponding weights as trained on RMG data, for nodules that appear in non-opaque and opaque regions of the lung respectively. After application of the WCI filter on the local contrast enhanced chest radiographs, coordinates that are likely to be nodules are further selected using methods described in Section 2.3.

Weighted multi-scale convergence index (WMCI) detector

The WMCI detector is a recent variation of the CI detector proposed in [7], an extension of the WCI detector This thesis attempts to optimize the the WCI detector using genetic algorithms. However, the possibility of detecting the optimal set of weights that would detect all nodule variations to involve pathology, size and subtlety is uncertain. The WMCI

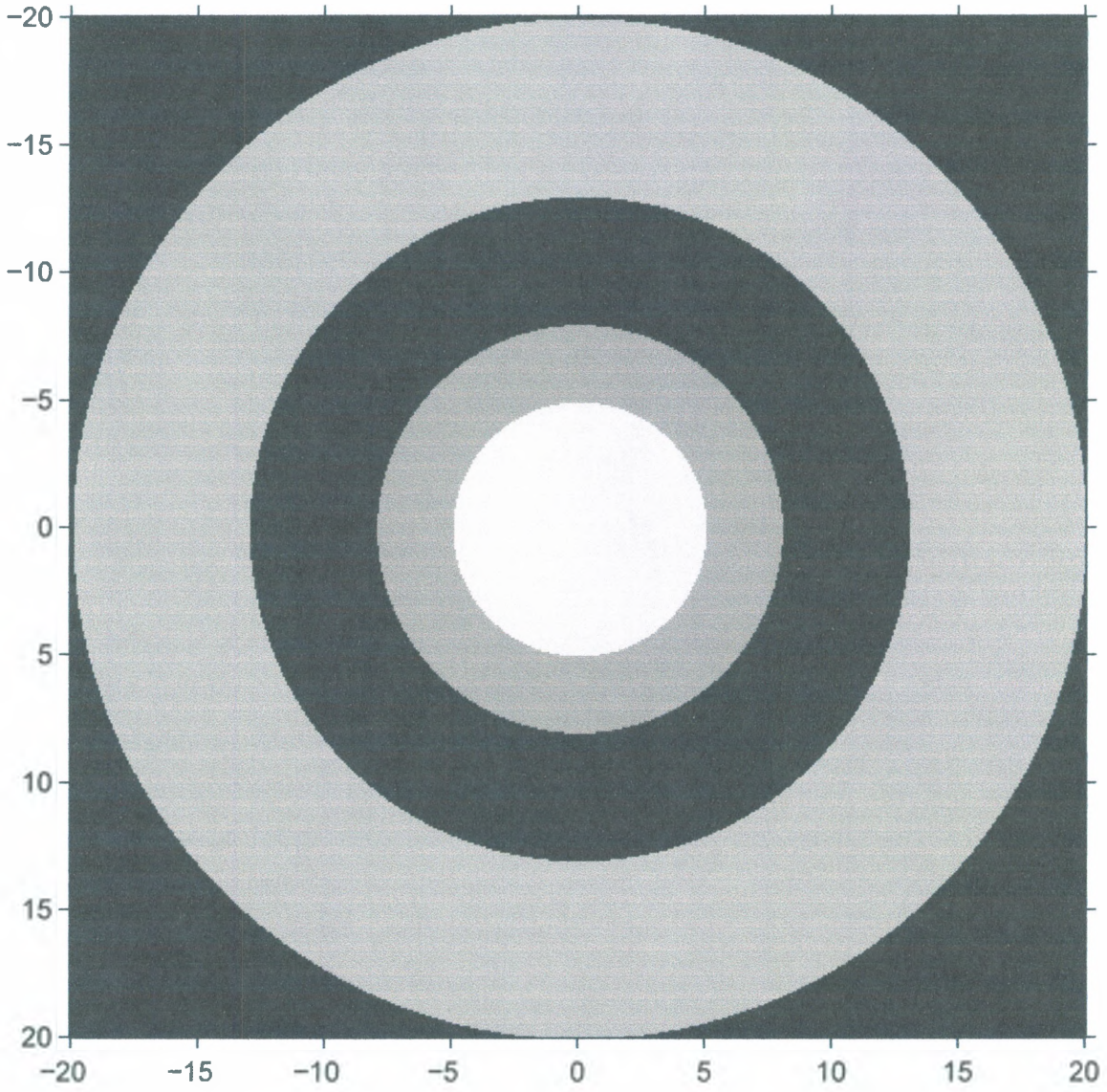

Figure 2.9: WCI filter depth map showing radii values that performed best when tested on RMG data with nodules that appear in the non-opaque region of the lung. Brighter regions corresponds to higher weight.

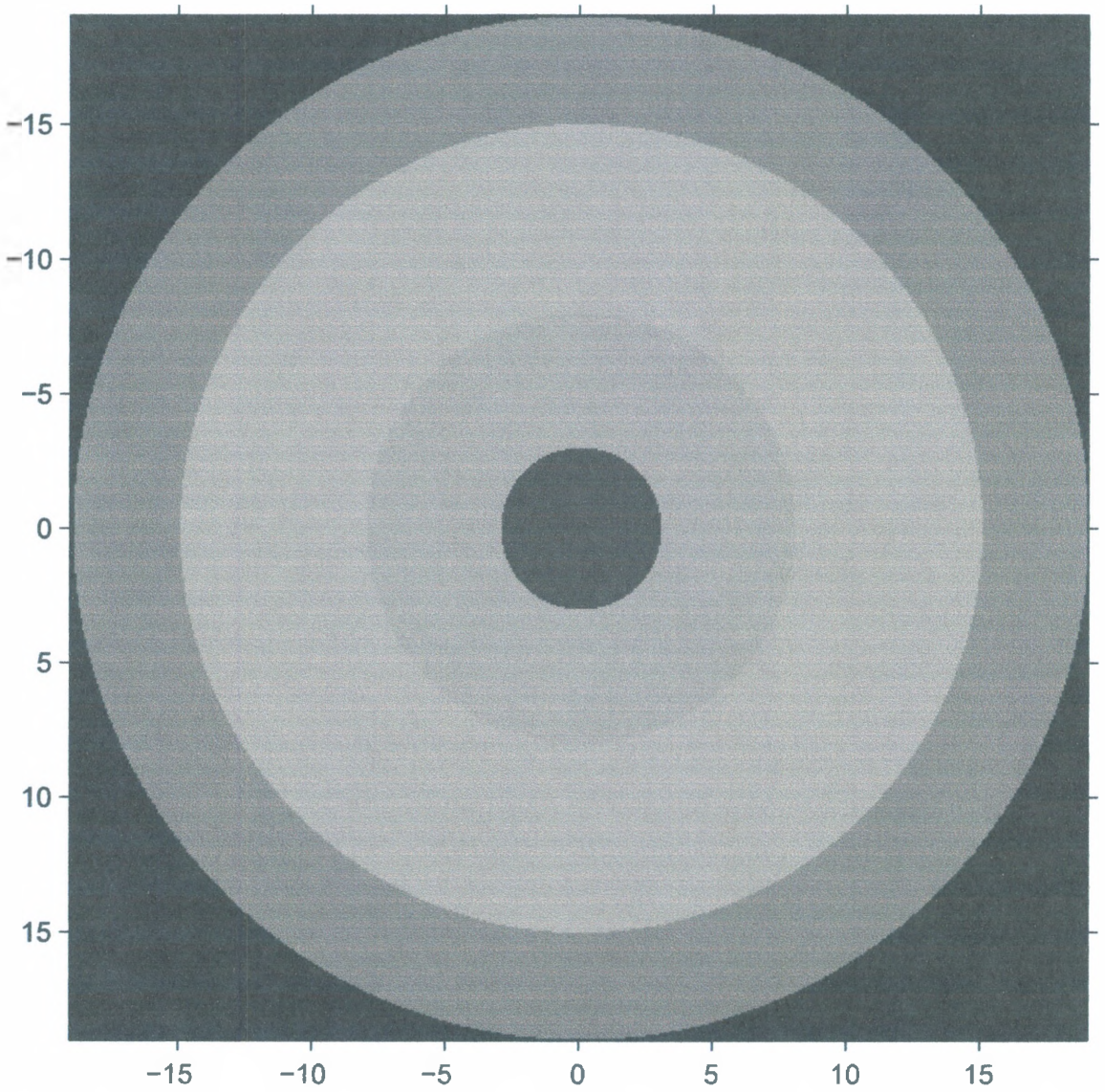

Figure 2.10: WCI filter depth map showing radii values that performed best when tested on RMG data with nodules that appear in the opaque region of the lung. Brighter regions corresponds to higher weight.

detector computes multiple WCI images and selects the maximum of these at each pixel. The WMCI value is computed as

$$WMCI(m,n) = \arg\max_{j} \left\{ \sum_{(k,l)\in M} w_j(k,l) \cos\left(\theta_{m,n}(k,l)\right) \right\}, \tag{2.9}$$

where $w_j(k,l)$ are the weights for the j'th scale WCI filter.

The WMCI detector is also trained using genetic algorithms to select 4 optimal radii and corresponding weight scales for the training data. The WMCI detector is trained, using genetic algorithms as described in Chapter III, to optimize tuning parameters for the non-opaque and opaque regions of the lung independently. Figure 2.11 shows a depth map of the scales and weights generated for the WMCI detector by genetic algorithms for for nodules in the non-opaque region of the lung. The scales are defined by the 4 outer radii of the filter. The depth map for the optimal filter scales with corresponding weight scales for nodules that appear in the opaque region of the lung is depicted in Figure 2.12

After application of the WMCI filter on the local contrast enhanced image, 4 filtered images are generated. The pixels with the maximum value is selected over all the scales for an output WMCI filtered image. Moreover, coordinates of the filtered image that are likely to be nodule candidates are further selected using postprocessing methods described in Section 2.3

2.3 Detection filter postprocessing

Each of the candidate detection filters is applied to the chest radiograph. Candidate detections are given by the pixels in this detection filtered image that are above a given

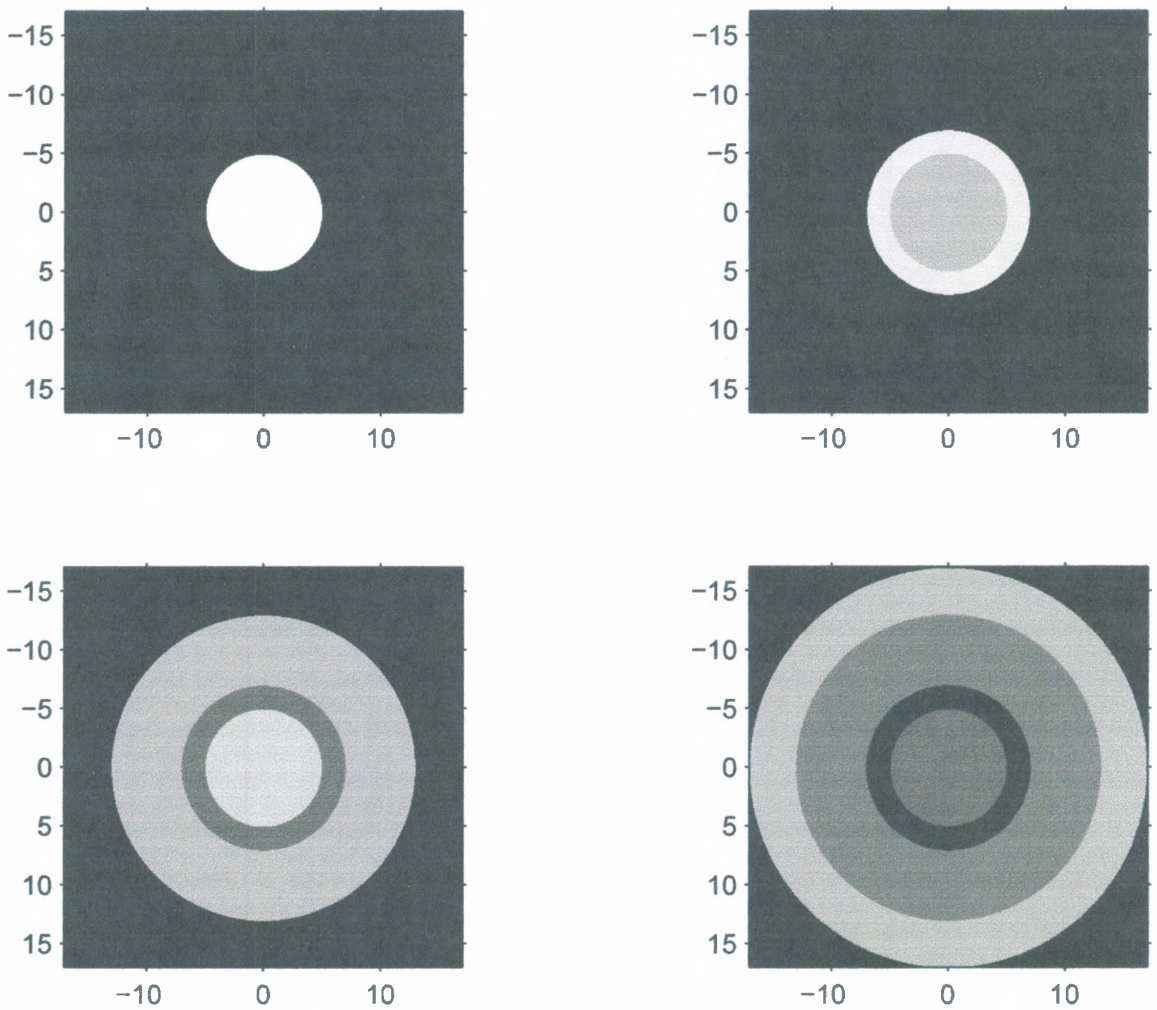

Figure 2.11: WMCI filter depth map showing scales that performed best when tested on RMG data with nodules that appear in the non-opaque region of the lung. Scales with brighter regions corresponding to higher weight. Each scale is defined by the radius of the outer circle.

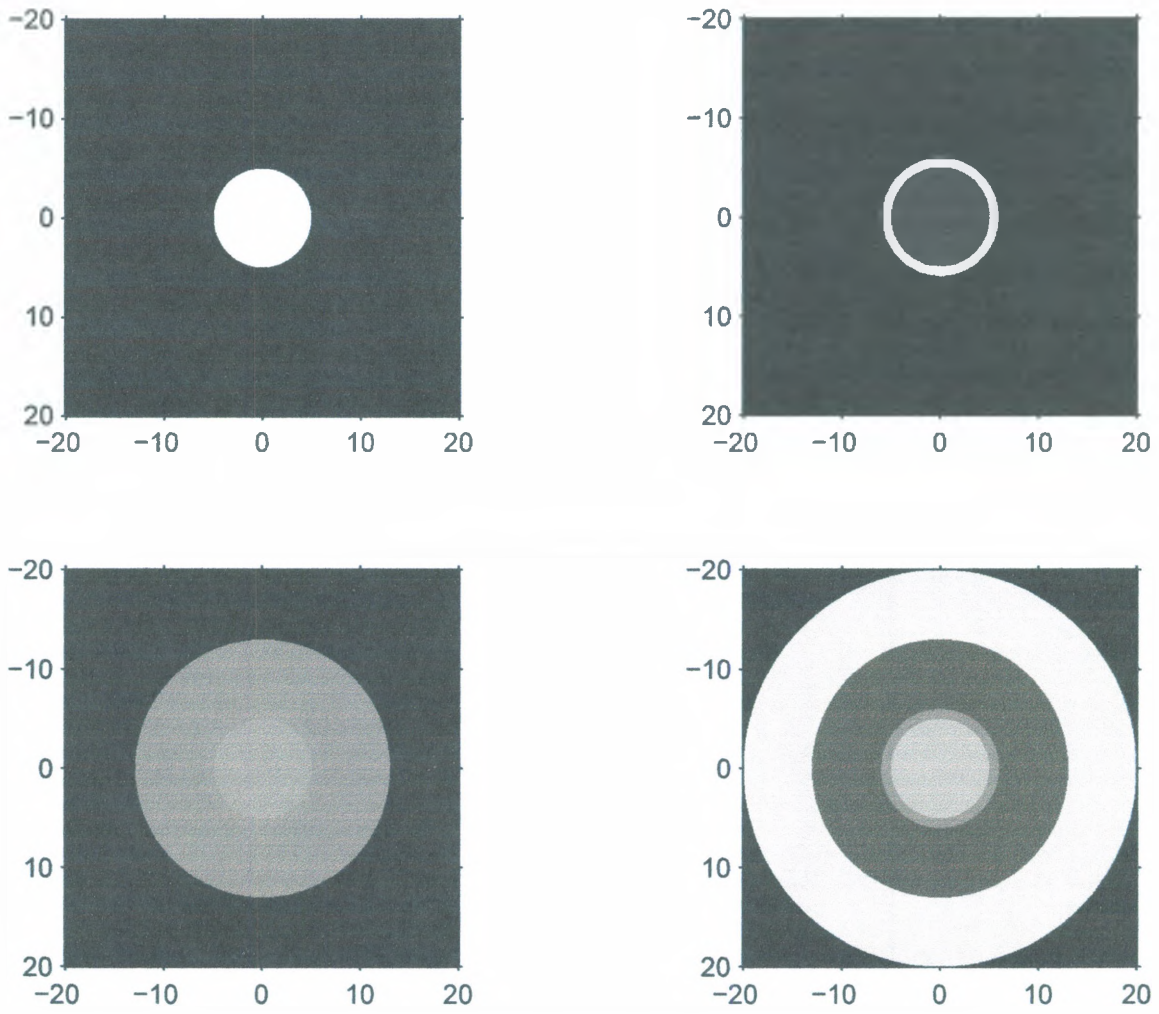

Figure 2.12: WMCI filter depth map showing scales that performed best when tested on RMG data with nodules in the opaque region of the lung. Scales with brighter regions corresponding to higher weight. Each scale is defined by the radius of the outer circle.

threshold, are local maxima, and are located within the appropriate segmented lung region on the chest radiograph (either opaque or non-opaque lung regions as described in Chapter I). The local maxima is computed by selecting connected components of pixels with the same intensity value in a 8×8 block neighborhood, whose external boundary pixels has lesser values. Using this process, the candidate detectors still generally produce a large number of detections. Moreover, many detections may be present on a single nodule or other anatomical structure. Therefore to help reduce the number of detections, we employ a detection thinning rule for all of the candidate detectors. In this detection thinning process, if detections lie within 5 mm of one another, only the detection with the higher pixel value is retained.

2.4 Labeling and scoring

The detectors are scored by comparing final output detection pixels of the detectors with the available radiologist truth information. The Riverain Medical and JRST datasets both contain coordinates (or cue points) specifying the locations of the approximate centers the nodules in each chest radiograph, as evaluated by radiologists. The approximate radius of each nodules is also provided in the radiologist truth information (but not the full segmentation boundary). In this work, we considered two detection labeling methods. In the first, we label a detection pixel a true positive (TP) if the detection lies within the radiologist provided radius of a cue point. If more than one detection lies within the truth radius of a cue point, we only credit the detector with one true positive detection for that particular nodule. Detections beyond the truth radius of a cue point are labeled as false positives (FP). For the second labeling method, we manually segmented all of he nodules

guided by the radiologist provided cue point and radius. Now, we label a detection a TP if it lies within a carefully drawn manual segmented nodule mask and label it an FP if it is outside the mask. Again, multiple detections within a single mask are only counted as one TP. We have observed that labeling based on the truth radius may not always be appropriate as nodules are sometimes irregularly shaped and far from circular. Thus, our results in Chapter IV focus on the use the manual segmentation based labeling. The detector performance is evaluated using free receiver operating characteristic (FROC) curves which plot the fraction of nodules detected (have a corresponding TP detection) versus the number of FPs per case. Each point on the FROC curve is generated by using a different threshold on the detection filtered image. A higher threshold produces lower sensitivity but greater specificity.

CHAPTER III

Genetic Algorithm Optimization

The performance of the WCI and WMCI detectors described in this thesis is dependent on multiple tuning parameters. The search space generated by the combination of these tuning parameters is large, and there is no clear combination of the tuning parameters that would produce optimal results for all test data. Genetic Algorithms (GAs) have been shown to perform well in pattern recognition problems as demonstrated in [23–25]. GAs are capable of searching the tuning parameters space for values that would yield an approximate optimal performance of the nodule candidate detectors, that would be otherwise tedious or impossible with exhaustive search.

GAs simulate the evolutionary idea of natural selection, where unfavorable heritable traits become less common until they are no more as new generations emerge. Genetic algorithms optimization is an iterative process. Initially a population is generated randomly from the search space of candidate solutions encoded as strings of symbols called chromosomes. A fitness value is then assigned to each chromosome based on its performance in solving the problem. In the successive iterations the algorithm keeps traits of chromosomes that yield values close to the optimal solution, and removes those that perform poorly compared to the rest. The algorithm also allows for evolutionary processes such as *mutation* to introduce new traits that might improve performance, and *crossover* which combines

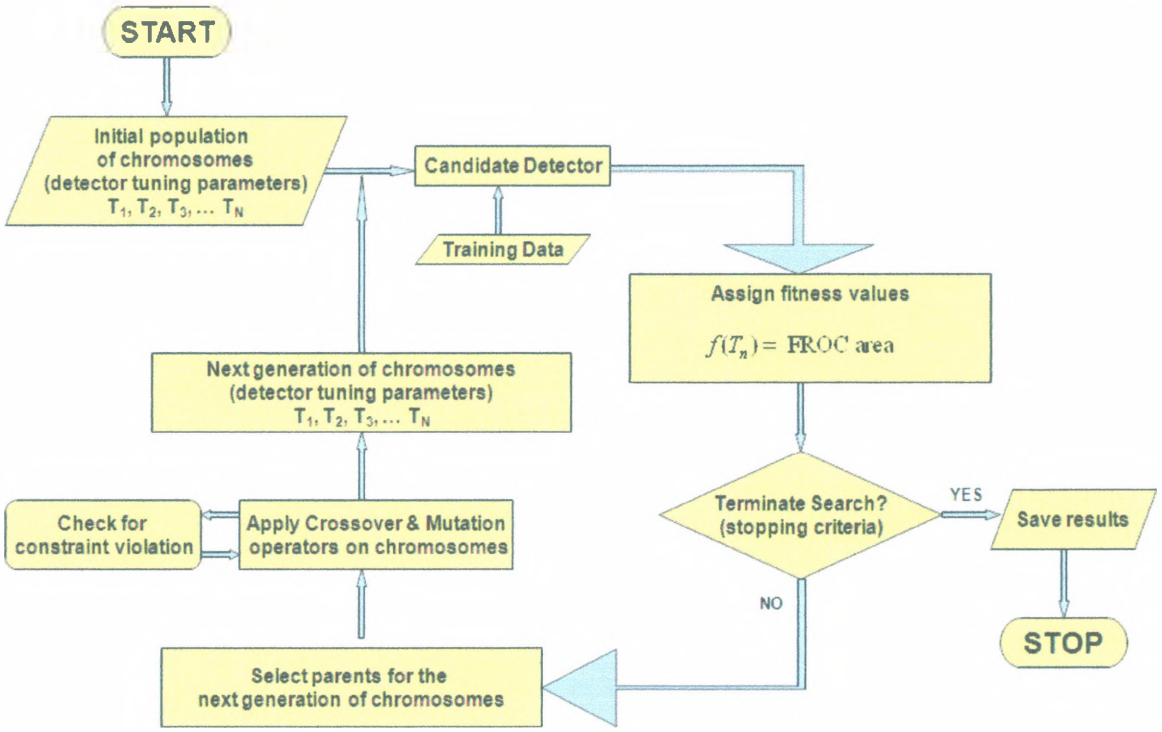

Figure 3.1: A block diagram describing the GA process used in optimizing the tuning parameters for the WCI and WMCI detectors.

the good traits from candidates with high fitness values to generate a better candidate. A block diagram of describing the GA process as applied to the WCI and WMCI detectors is shown in Figure. 3.1. The implementation of the main components of the GA algorithm are detailed below.

3.1 Fitness function

The fitness function evaluates the fitness the chromosomes in each generation. The chromosomes for the WCI detectors are setup by combining the radii and their corresponding weights. The threshold value and the minimum distance allowed between each

TUNING PARAMETERS	R_1	R_2	R_3	R_4	W_1	W_2	W_3	W_4
LOWER BOUND	1	6	11	16	-1	-1	-1	-1
UPPER BOUND	5	10	15	20	1	1	1	1

Table 3.1: Lower and upper limit constraints for the scales and weights that are used to train the WCI Detector where R_n and W_n represents nth radius and nth weight respectively.

detection are held constant. The WMCI detector chromosomes also combine different scales each with its corresponding weight vector while fixing the threshold value and the minimum distance allowed between each detection. The threshold value for the WCI and WMCI detectors are heuristically selected by trying different values and choosing the value with best average performance. The thresholds chosen are 0.2 for WCI detector and 0.5 for the WMCI detector. The threshold could be made variable to reduce the constraint on the GA. The WCI and WMCI detector filters have been trained using the chromosomes determined by the tuning parameters for each nodule candidate detector exclusively on the Riverain data.

The fitness function is setup to maximize the area under the FROC curve generated at each iteration. At each iteration a fitness value is assigned to each chromosome. Chromosomes that yield low FROC curve area are automatically assigned a fitness value of zero, which makes them have a very low survivability. These chromosomes will only be parent candidates for the next generation if there are no other existing chromosomes that yielded minimum required area under the FROC curve. This case usually occur at the first few iterations before the algorithm starts to converge. Tables 3.1 and 3.2 shows the setup of the the tuning parameters optimized for the WCI and WMCI nodule candidate detectors respectively.

RADII	R_1	R_2	R_3	R_4
LOWER BOUND	1	6	11	16
UPPER BOUND	5	10	15	20
-	-	-	-	
SCALE 1	1	0	0	0
SCALE 2	W_1	W_2	0	0
SCALE 3	W_3	W_4	W_5	0
SCALE 4	W_6	W_7	W_8	W_9

Table 3.2: Scales and weights used to train the WMCI Detector where R_n and W_n represents nth radius and nth weight respectively. The lower and upper bounds for the weights are -1 and 1 respectively.

3.2 Selection operator

The selection operator determines what chromosomes are considered for reproduction in the next generation. At each iteration the chromosomes are ranked according to their fitness values in descending order. The parents for the next generation of chromosomes are then chosen from the chromosomes with the highest ranks.

3.3 Reproduction

The initial population for the GA is randomly generated and the fitness values for each chromosomes is evaluated. However after the first generation, a reproduction process determines what chromosomes will be evaluated in the iteration. (i.e the next generation of chromosomes). First and foremost, a few of chromosomes corresponding to the best fitness values are chosen to survive to the next generation. Moreover some chromosomes are created by crossover, which involves combination of tuning parameters among the selected parents to form new chromosomes. A mutation function is used to make small random

changes in the individuals in the the next generation chromosomes to broaden the search space for the GA. The mutation function used is a Gaussian function that adds a random number from a distribution whose variance approaches zero as the GA converges. The next generation of chromosomes are tested for violation of the tuning parameter constraints before they are evaluated. The uppper and lower bounds of the constraints for the GA tuning parameters for the WCI and WMCI detectors are depicted in Tables 3.1 and 3.2 respectively.

3.4 Termination

Several factors determines the termination of the GA because there is no certainty as to how quickly the algorithm will converge. The algorithm comes to an halt after 100 iterations, or if the fitness values is not getting any better after 50 iterations.

CHAPTER IV

Experimental results

A performance analysis comparing each of the candidate detectors using the JRST database is presented in this chapter. We begin by presenting an analysis showing the performance of the candidate detectors on the 140 JRST nodule cases with nodules in the non-opaque region of the lung. A performance analysis of the candidate detectors on the 14 JRST nodules that appear in the opaque region of the lung is presented in the following section. Finally, an evaluation showing the performance of the WMCI detector combining detections in the opaque and non-opaque portions of the lung is presented.

4.1 Non-opaque regions of the lung

FROC curves for all of the evaluated nodule candidate detectors in non-opaque region of the lung are depicted in Figure 4.1. The 140 JRST images with nodules inside the non-opaque lung mask are used to generate these results. These results are based on manual nodule segmentation labeling as described in Section 2.4, where the nodule candidate detections are compared against the manually segmented nodule masks. Optimization of the tuning parameters for all the detectors is done exclusively using the independent RMG dataset. The Lindeberg, ARG, RCI and SDCI detectors tuning parameters are optimized with exhaustive search. The WCI and WMCI tuning parameters are optimized with the

optimization methods described in Section III. Note that the CI based detectors outperform the Lindeberg blob detector and the ARG detector, with the SDCI, WCI, and WMCI nodule candidate detectors taking the lead.

The result of the nodule candidate detectors are similar to results reported in literature where the same JRST images are used to test the performance of the nodule candidate detectors. When we include the 14 nodules that appear in the opaque region of the lung in testing the overall performance of the nodule candidate detectors, a total number of 28490 candidates are detected at 85.72% sensitivity with the Lindeberg blob detector which is comparable to the the results of [2] where 33073 nodules candidates are detected with 86.4% sensitivity on the 154 (140 non-opaque and 14 opaque) nodule cases in the JRST data. The WMCI yielded 95.7% sensitivity with average number of FPs per image of 96.9% with truth radius scoring and this result is similar to [7], where 95% of the nodules have a WMCI detection within their truth radius with average detections per image of 97.2 detections.

4.2 Opaque regions of the lung

Nodules that appear in the opaque region of the lung tend to be much more difficult to detect. This is because the generally exhibit lower contrast with respect to their surroundings and tend to have more varied shapes and textures. Here we evaluate the ability of the detectors to locate the 14 opaque region nodules in the JRST dataset. Figure 4.2 shows the FROC curves for the detectors with regard to the opaque region nodules. As before, the tuning parameter optimization has been done exclusively with independent RMG training data. However, two training procedures are used giving rise to two FROC curves for each

detector. The curves labeled TOTO (train on opaque and test on opaque) correspond to training only only the 7 RMG opaque nodules. Since this training set may be too small to yield reliable parameter optimization results, we separately used the the non-opaque nodules for training from the RMG dataset and then applied the resulting detectors to the opaque nodules in JRST. The FROC curves for this method are labeled TNTO (train on non-opaque and test on opaque).

Note that the Lindeberg detector outperforms other detectors for TNTO yielding 100% sensitivity with 30.43 average false positives per image. The results of the Lindeberg, SDCI, RCI and WMCI detectors are comparable overall(similar area under FROC curve) and better than the ARG and WCI detectors when the tuning parameters obtained from training on the non-opaque data. The Lindeberg, SDCI, RCI and WMCI detectors are able to detect all 14 of the JRST nodules in the opaque region with an average of 40.1, 45.9, 36.1, and 54 FPs per image, respectively. At 92.86% sensitivity the Lindeberg, SDCI, RCI and WMCI yielded 28.43, 30, 22.2, 25.3 FPs per image, respectively. Hence the RCI detector takes the lead when non-opaque region data is used for training.

4.3 Overall WMCI detector performance

The opaque and non-opaque regions of the lung are mutually exclusive and have very different characteristics. Thus, different detectors can be applied to each region with independent tuning parameters and operating points (thresholds on the detection filtered images). However, the performance of a system containing two detectors (one for opaque nodules regions and one for non-opaque regions) can be captured with a 3D FROC curve as shown in Figure 4.3. This FROC curve is for the WMCI detector trained on the RMG

data (non-opaque) and applied to the JRST (opaque and non-opaque). Every point on this surface corresponds to a particular combination of operating points for the two detectors. The height represents the overall sensitivity of the two detectors together (the fraction of all nodules, opaque and non-opaque, detected by either detector). One horizontal axes represent the number of FPs generated by one detector operating in the opaque regions of the lung. The other horizontal axis shows the number of FPs generated by the other detector operating on the non-opaque region of the lung. By adding the two horizontal axis values, one gets the total number of FPs for this combined detector system. For example, if we choose to operate at 96.9% average FPs per image in non-opaque region and 25.3% average FPs per image in opaque region, the overall sensitivity of the combined system would be 95.45% as shown in Figure 4.3.

We believe this 3D FROC curve is a helpful way to visualize the possible operating points for a two detector system. Note this this curve clearly shows that to get a high sensitivity with a relatively small number of FPs, one might choose to only operate on the non-opaque regions (0 FPs in opaque, with 0 detections in opaque). In fact, this is how many CAD systems have been presented [2, 7]. However, this system will always miss the 14 nodules in the opaque region. In order to pick those up, one needs to also employ an opaque region detector, moving the operating point from the edge of the curve into its interior.

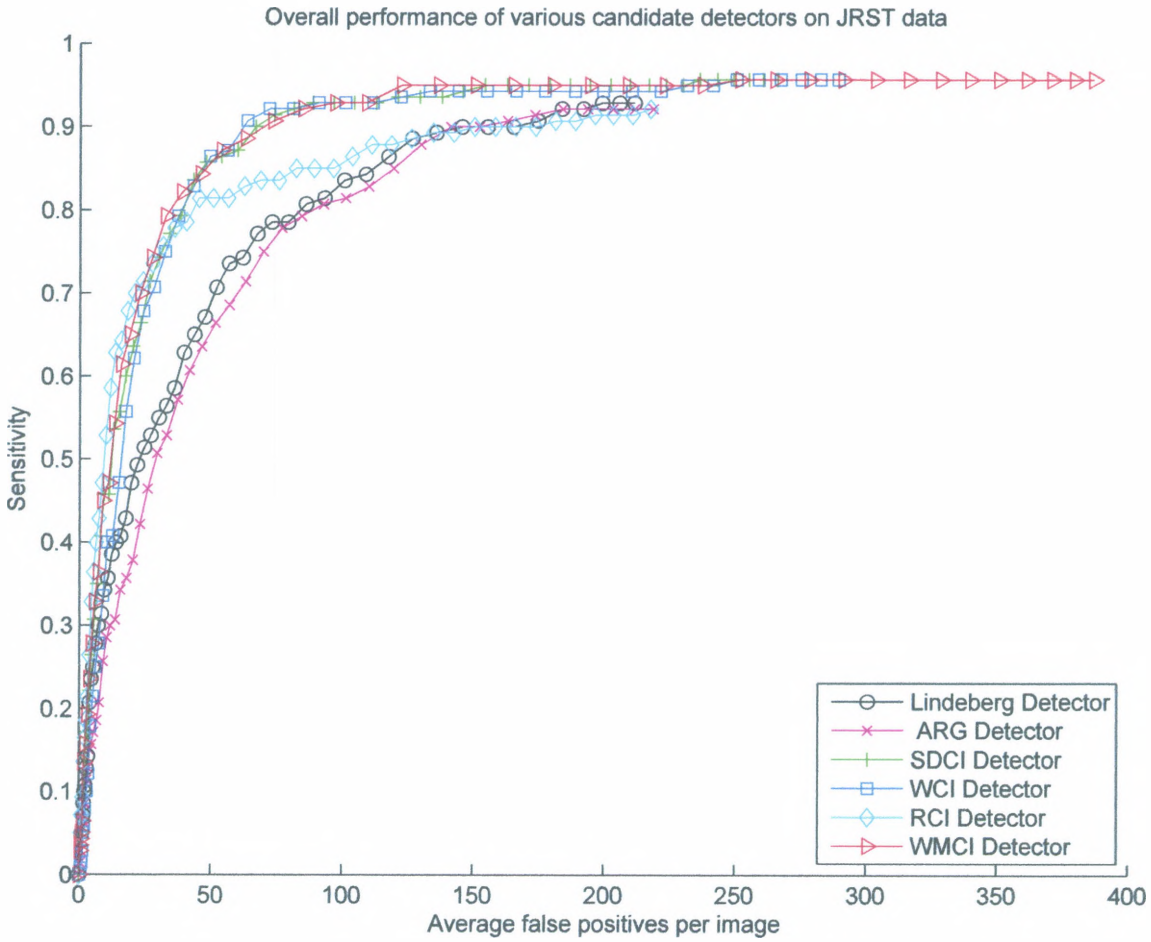

Figure 4.1: Comparison of FROC curves for all detectors as tested on JRST data with nodules in non-opaque regions of the lung. These FROC curves are generated using manual nodule segmentation labeling.

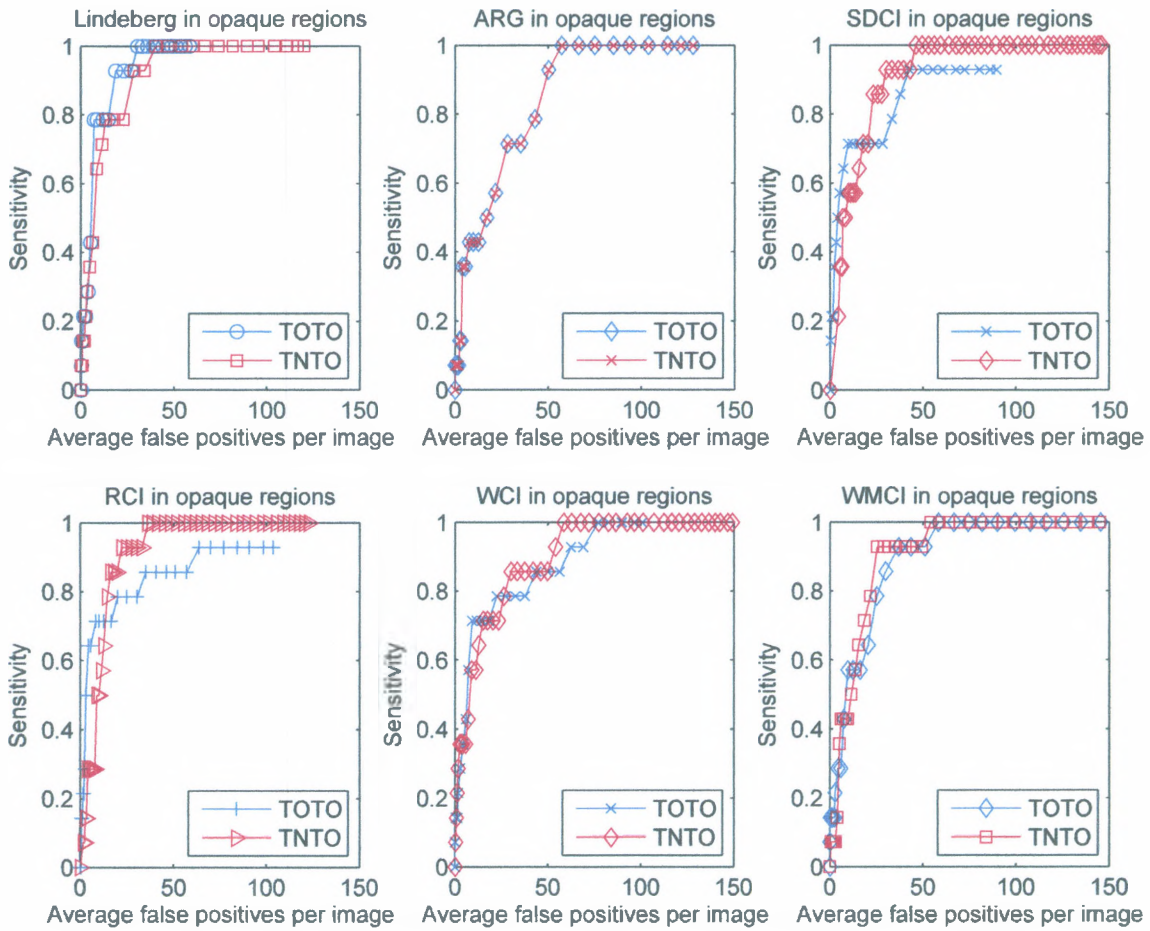

Figure 4.2: FROC curves for the detectors operating in the opaque region of the lung as tested on JRST data. The truth radius labeling method is used here for scoring. TOTO implies train on opaque region nodules and test on opaque region nodules. TNTO implies train on non-opaque data and test on opaque region data.

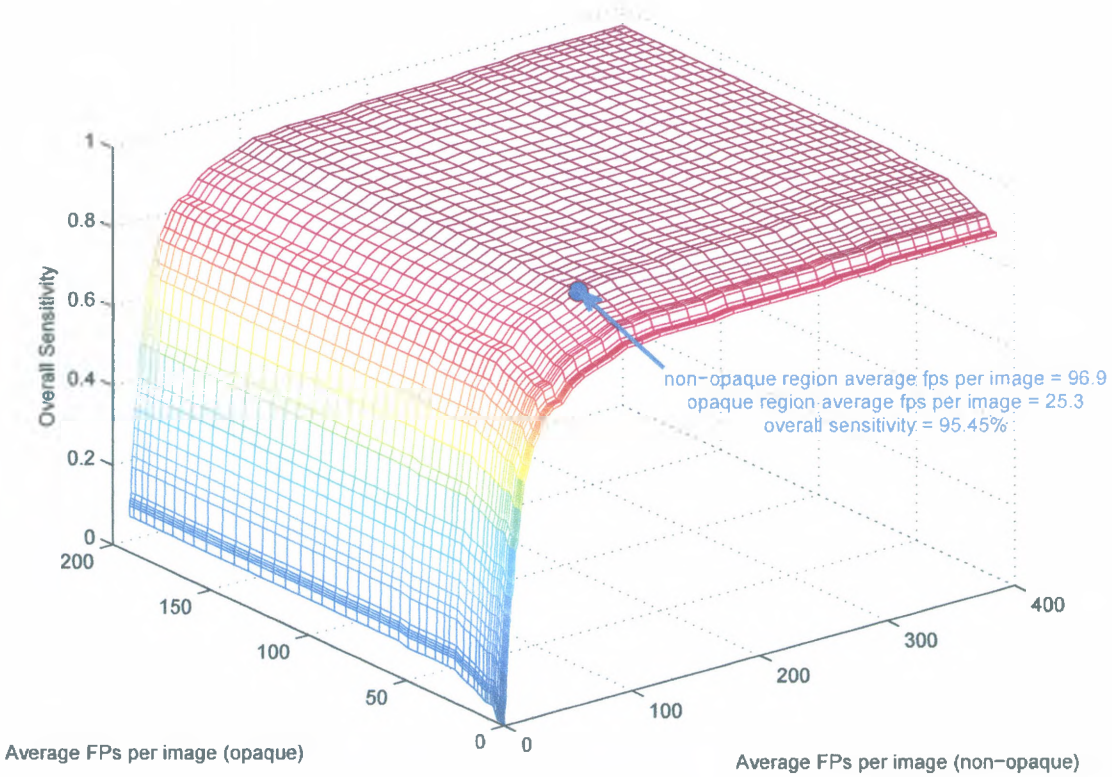

Figure 4.3: 3D FROC curve for the dual WMCI detector (opaque and non-opaque). Every point on this surface corresponds to a particular combination of operating points for the two detectors. The height represents the overall sensitivity of the two detectors together. One horizontal axes represent the number of FPs generated by one detector operating in the opaque regions of the lung. The other horizontal axis shows the number of FPs generated by the other detector operating on the non-opaque region of the lung.

CHAPTER V

Conclusion

A smart choice of the appropriate blob detector for an application significantly reduces the number of regions where features are computed in the image, as features are computed only on regions that are most likely to be of interest. Moreover, the work load of the classifier in the pattern recognition system is also reduced as fewer candidate segments are classified compared to the whole image. In medical applications such as detection of nodules in chest radiographs a great number of false detections are eliminated in the CAD system with the choice of an appropriate candidate blob detector to select initial nodule candidates in chest radiographs. In this thesis, a formal comparison among the nodule candidate detectors used for selecting initial nodules in chest radiographs has been presented. The results can also be used as a guidance for selecting detectors for other blob detection applications in pattern recognition. A genetic algorithm method for optimizing blob detectors requiring several tuning parameters has also been presented. We have also addressed the detection of blobs that appear in the opaque region of the lung. We have also shown that combination operating points in the non-opaque and opaque region of the lung can be achieved from the prior probabilities of each region to reduce the large false positives that may be generated in CAD system as a result of inclusion of the opaque region performance as shown in Figure 4.3.

This comparative study shows that the SDCI, WCI and WMCI detectors, which are all CI based detectors, are better in detecting nodules that appear in the non-opaque region of the lung than Lindeberg, ARG and RCI detectors. The CI based detectors does not take gradient magnitude into consideration when computing convergence index values, as a result, there is increase detection of blobs with different variation in texture and shape and blobs that has close intensities to its surrounding region. For nodules that appear in the opaque regions of the lung the Lindeberg, SDCI, RCI and WMCI detectors outperform other detectors with the ability to detect the nodules in the opaque regions with fewer false detections. From Figures 4.1, 4.2 it is apparent that the SDCI, and WMCI detectors perform well in detecting nodules both in opaque regions and non-opaque regions of the lung. Though the Lindeberg detector yielded good results in the opaque region of the lung, it has the worst performance in the non-opaque region of the lung. For other pattern recognition applications where there is a need for blob detection, the WMCI detector in recommended over the other detectors evaluated in this thesis because of its ability to take the form of other CI based detectors (such as the SDCI detector which yielded similar results to the WMCI detector in both regions of the lung). In many pattern recognition application problems, blobs appear at different scales. With the WMCI detector the tuning parameters can be automatically selected to fit the scales present in application at hand using the genetic algorithm optimization method presented in this thesis.

BIBLIOGRAPHY

[1] J. Shiraishi, Q. Li, K. Suzuki, R. Engelmann, and K. Doi, "Computer-aided diagnostic scheme for detection of lung nodules on chest radiographs: Localized search method based on anatomical classification," *Medical Physics*, vol. 33, no. 7, pp. 2642–2653, July 2006.

[2] A. Schilham, B. van Ginneken, and M. Loog, "A computer-aided diagnosis system for detection of lung nodules in chest radiographs with an evaluation on a public database," *Medical Image Analysis*, vol. 10, no. 2, pp. 247–258, 2006.

[3] ——, "Multi-scale nodule detection in chest radiographs," in *Medical Image Computing and Computer-Assisted Intervention*, ser. Lecture Notes in Computer Science, R. Ellis and T. Peters, Eds., vol. 2878. Springer, 2003, pp. 602–609.

[4] J. Wei, Y. Hagihara, and H. Kobatake, "Detection of rounded opacities on chest radiographs using convergence index filter," in *ICIAP '99: Proceedings of the 10th International Conference on Image Analysis and Processing*. Washington, DC, USA: IEEE Computer Society, 1999, p. 757.

[5] ——, "Detection of cancerous tumors on chest x-ray images candidate detection filter and its evaluation," in *ICIP (3)*, 1999, pp. 397–401.

[6] M. T. Freedman, S.-C. Lo, T. Osicka, F. Y. Lure, X.-W. Xu, J. Lin, H. Zhao, and R. Zhang, "Computer-aided detection of lung cancer on chest radiographs: effect of machine cad false-positive locations on radiologists' behavior," in *Proceedings of SPIE, Medical Imaging*, vol. 4684, May 2002, pp. 1311–1319.

[7] R. C. Hardie, S. K. Rogers, T. Wilson, and A. Rogers, "Performance analysis of a new computer aided detection System for Identifying Lung Nodules on Chest Radiographs," *Medical Image Analysis*, 2007.

[8] T. Lindeberg, "Detecting Salient Blob-Like Image Structures and Their Scales with a Scale-Space Primal Sketch: A Method for Focus-of-Attention," *International Journal of Computer Vision* , vol. 11, no. 3, pp. 283–318, 1993.

[9] ——, "Feature detection with automatic scale selection," *International Journal of Computer Vision*, vol. 30, no. 2, pp. 77–116, 1998.

[10] H. Chang, Q. Yang, and B. Parvin, "Segmentation of heterogeneous blob objects through voting and level set formulation," *Pattern Recogn. Lett.*, vol. 28, no. 13, pp. 1781–1787, 2007.

[11] L. Bretzner and T. Lindeberg, "Feature Tracking with Automatic Selection of Spatial Scales," *Computer Vision and Image Understanding* , vol. 71, pp. 385–392, 1998.

[12] H. Bay, T. Tuytelaars, V. Gool, and L., "Surf: Speeded up robust features," in *9th European Conference on Computer Vision*, Graz Austria, May 2006.

[13] T. Lindeberg and J. Garding, "Shape-adapted smoothing in estimation of 3-d depth cues from affine distortions of local 2-d brightness structure," in *Proc 3rd European Conference on Computer Vision, ECCV'94*, 1994, pp. 389–400.

[14] D. Lowe, "Distinctive image features from scale-invariant keypoints," in *International Journal of Computer Vision*, vol. 20, 2003, pp. 91–110.

[15] K. Mikolajczyk and C. Schmid, "An affine invariant interest point detector," in *ECCV (1)*, 2002, pp. 128–142.

[16] G. G. H. Sossa, F. Cuevas and O. Pogrebnyak, "Improved technique to determine the number of blobs in an image," in *Visualization, Imaging, and Image Processing* , 2002.

[17] J. K. Gohagan, P. M. Marcus, R. M. Fagerstrom, P. F. Pinsky, B. S. Kramer, P. C. Prorok, S. Ascher, W. Bailey, B. Brewer, and T. Church, "Final results of the lung screening study, a randomized feasibility study of spiral ct versus chest x-ray screening for lung cancer," *Lung Cancer*, vol. 47, no. 1, pp. 9–15, January 2005. [Online]. Available: http://dx.doi.org/10.1016%2Fj.lungcan.2004.06.007

[18] B. van Ginneken, B. ter Haar Romeny, and M. Viergever, "Computer-aided diagnosis in chest radiography: a survey," *IEEE Transactions on Medical Imaging*, vol. 20, no. 12, pp. 1228–1241, 2001.

[19] B. van Ginneken, M. Stegmann, and M. Loog, "Segmentation of anatomical structures in chest radiographs using supervised methods: a comparative study on a public database," *Medical Image Analysis*, vol. 10, no. 1, pp. 19–40, 2006.

[20] A. Schilham and B. van Ginneken, "Computer-aided diagnosis as a second reader for nodule detection in chest radiographs versus single and double reading," in *European Congres of Radiology*, 2005, p. 205.

[21] H. Kobatake and S. Hashimoto, "Convergence Index Filter for Vector Fields," *IEEE Transcations on Image Processing*, vol. 8, no. 8, 1999.

[22] G. Coppini, S. Diciotti, M. Falchini, N. Villari, and G. Valli, "Neural networks for computer-aided diagnosis: detection of lung nodules in chest radiograms," *IEEE Transactions on Information Technology in Biomedicine*, vol. 7, no. 12, pp. 344–357, Dec. 2003.

[23] J. Wei, Y.Hagihara, A.Shimizu, and H.Kobatake, "Optimal image feature set for detecting lung nodules on chest x-ray images," in *Proceedings CARS*, 2002, pp. 706–711.

[24] M. Pei, E. Goodman, and W. Punch, "Feature extraction using genetic algorithms," 1997. [Online]. Available: citeseer.ist.psu.edu/pei97feature.html

[25] S. Forrest, R. E. Smith, B. Javornik, and A. S. Perelson, "Using genetic algorithms to explore pattern recognition in the immune system," *Evolutionary Computation*, vol. 1, no. 3, pp. 191–211, 1993. [Online]. Available: citeseer.ist.psu.edu/article/forrest92using.html